Resistance Spot Welding of Heat-Treatment-Free Die-Casting Aluminum Alloy

The effects of preheating and postheating current on joint performance were investigated with Newton ring electrodes

BY Y. ZHU, Y. WANG, J. BAI, B. ZENG, Z. ZHU, AND S. YANG

Abstract

The application of heat-treatment-free cast aluminum alloys in automotive structural parts is increasing, but their weldability is still unclear. This paper explores the resistance spot welding (RSW) of the heat-treatment-free die-casting aluminum alloy C611 utilizing an innovative welding electrode integrated with preheating and postheating techniques. The single pulse, preheating, and postheating pulse processes were designed. Moreover, the effects of the welding procedure on the weld's morphology, microstructure, and properties were compared and analyzed. Results showed that the single pulse welding process was prone to generating weld defects such as internal porosity and expulsion, and the joint strength was relatively low. By applying proper preheating and postheating pulses, welding defects could be effectively suppressed, and the width of the columnar fine grain zone could be reduced, which improved the performance of the equiaxed grain zone (EGZ) by 20%. The weld's tensile shear performance and energy absorption were increased by 11.7% and 38.3%, respectively. Furthermore, the optimized electrode's unique shape helped stabilize the size of the nugget's EGZ.

Keywords

- Heat-Treatment-Free Die-Casting Aluminum Alloy
- Resistance Spot Welding
- Electrode
- Current Impulse
- Microstructure
- Weld Performance

https://doi.org/10.29391/2025.104.006

Introduction

With the development of the automobile industry, the consumption of fossil fuels has increased dramatically, which has led to an increase in greenhouse gas emissions (Refs. 1, 2). Reducing fuel consumption and improving fuel efficiency is one of the effective ways to reduce greenhouse gas emissions. Reducing vehicle weight and improving engine efficiency can effectively reduce fuel consumption. In general, for every 10% reduction in vehicle weight, fuel consumption can be reduced by 3–7%. In addition, using aluminum alloys can reduce 13–20 kg of greenhouse gas emissions per kilogram (Refs. 1–5). Aluminum alloys have become an ideal replacement for steel because of their low density and high specific strength ratio. In the automotive industry, they can reduce vehicle weight by 50% compared to traditional materials without affecting the stability and safety of the body (Ref. 6). Therefore, they are expected to replace steel as the primary material in the automotive industry (Refs. 7, 8). By 2025, the amount of aluminum alloy used in automobiles will be as high as 250 kg/vehicle, nearly 80% of which will be cast aluminum alloy (Ref. 9).

Heat-treatment-free cast aluminum alloy is a new type of aluminum alloy material that has been developed in recent years. High strength and plasticity can be achieved without high-temperature solution treatment and artificial aging (Ref. 10). The heat-treatment-free cast aluminum alloys are mainly divided into Al-Si series and Al-Mg series alloys (Refs. 11, 12). Cast aluminum alloys are used primarily to manufacture engine cylinder blocks, cylinder heads, clutch shells, bumpers, wheels, and chassis components (Refs. 13, 14).

Most research on cast aluminum alloys focuses on their manufacturing and forming processes. It is indispensable to investigate the weldability of cast aluminum alloys. However, only limited research has been conducted on welding them. Akhter (Ref. 15) studied the effect of post-weld heat treatment on cast aluminum A356 laser welds. Due to the fine dendritic structure formation in the weld, the mechanical properties of the weld are better than base metal. Using high-temperature treatment, the welds' yield strength and ultimate tensile strength were further improved compared

to those without high-temperature treatment and as-cast samples. Although the post-weld heat treatment improved the mechanical properties of the weld, it reduced production efficiency. Therefore, the automotive industry keeps looking for new welding approaches to reduce manufacturing costs and improve productivity. Reisgen (Ref. 16) studied the atmospheric electron beam welding of aluminum die-casting alloy AlSi10MnMg. It was found that the porosity of the weld could be controlled by optimizing the hydrogen content in the casting aluminum alloy and adjusting the welding speed. However, this welding process is complex and unsuitable for mass production. Scheibner (Ref. 17) accomplished gas metal arc welding of die-casting aluminum alloy thin-walled parts. Vivas (Ref. 18) used friction stir welding in Al-Si cast aluminum and Al-Mg cast aluminum alloy. Although the formation of the weld defects could be significantly reduced, the ultimate tensile strength of the welded joints was also lower.

Resistance spot welding (RSW) is the dominant automotive body structure manufacturing process due to its robustness, high productivity, low cost, and flexibility (Refs. 19, 20). Compared with laser welding, electron beam welding, arc welding, and friction stir welding, RSW is under electrode force during the whole welding process, which allows it to overcome the weld's shrinkage and porosity. Welding electrode (Ref. 21) and current input form (Refs. 22, 23) have an essential influence on the weld quality of aluminum alloy. In the early stage, we developed (Ref. 24) a welding electrode called a Newton ring (NTR) electrode (Refs. 23, 25), which could inhibit the expulsion of aluminum alloy, reduce welding current and electrode wear, and

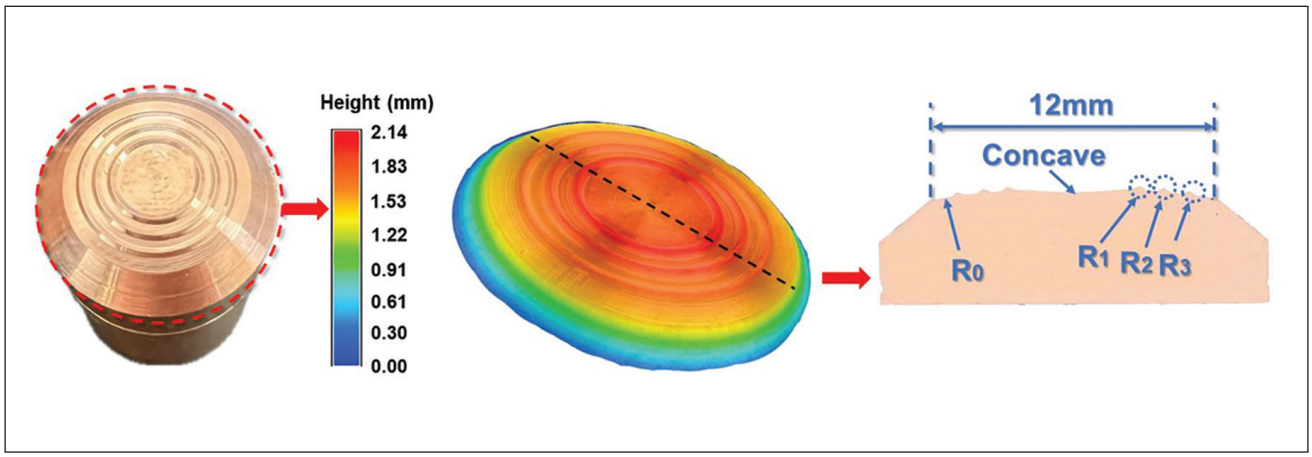

Fig. 1 — Electrode appearance and cross-section size.

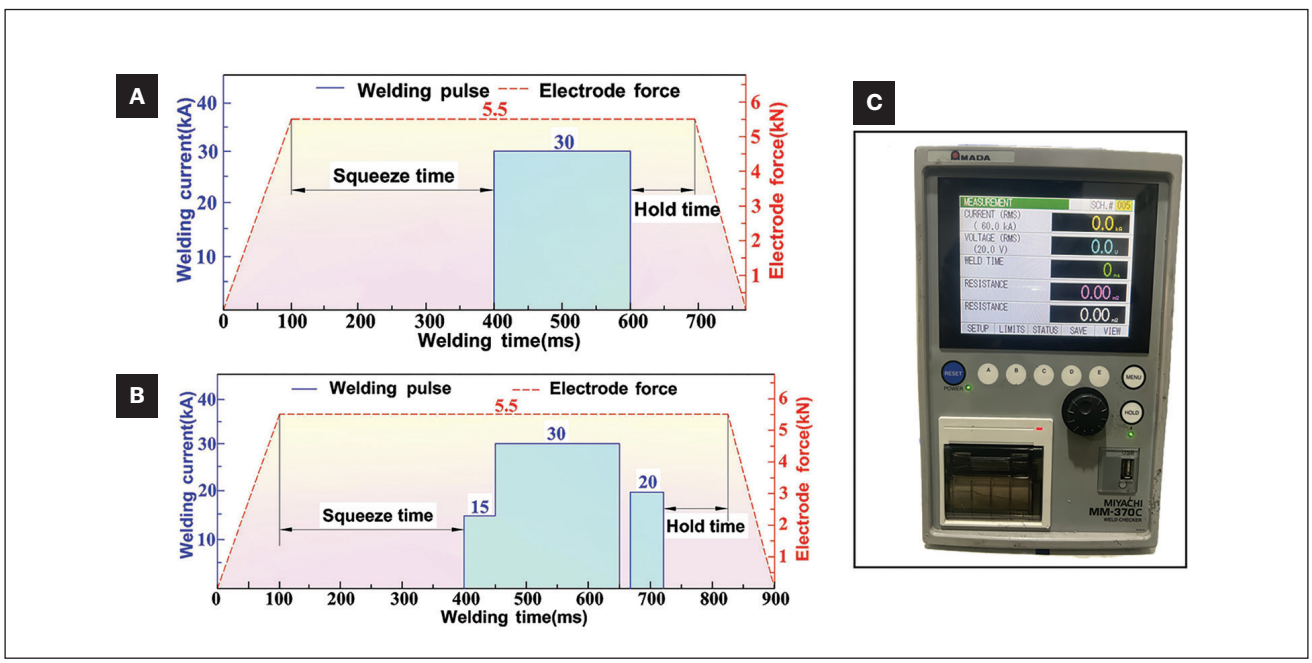

Fig. 2 — Welding schedule and controller: A — Process 1 welding schedule; B — Process 2 welding schedule; C — welding controller.

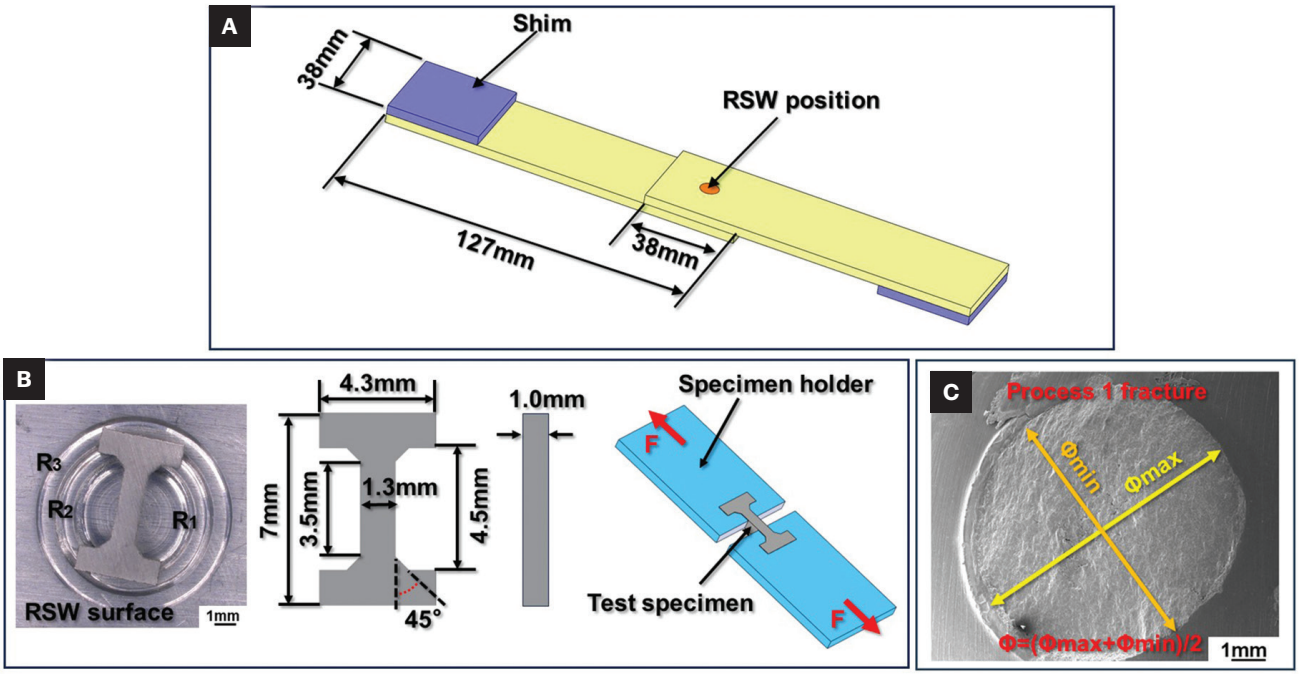

Fig. 3 — Tensile specimen size: A — Tensile shear specimen size; B — micro-tensile specimen size; C — measurement method of nugget diameter.

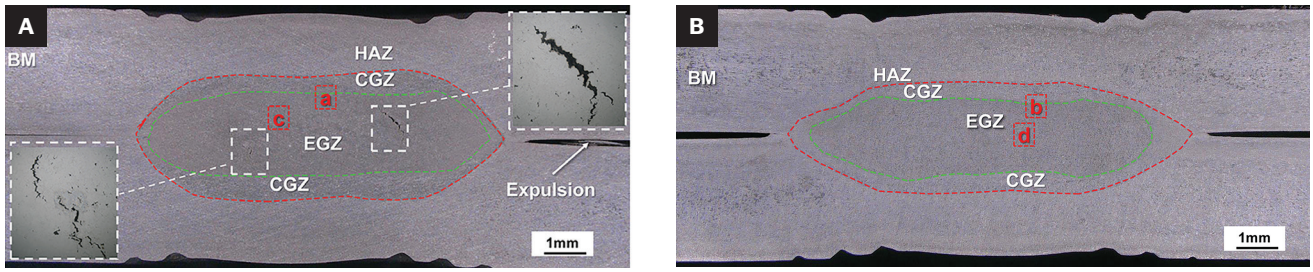

Fig. 4 — The nugget morphology with two processes: A — Process 1; B — Process 2.

Table 1 — Chemical Composition and Mechanical Properties of C611

Si	Mn	Mg	Fe	Zr	Ti	Sr	Al	Yield Strength (MPa)	Tensile Strength (MPa)	Elongation (%)
7.12	0.61	0.21	0.15	0.05	0.1	0.008	Bal.	99	255	12.4

improve the stability of the welding process. Different from General Motors's Multi-Ring Domed (MRD) electrode (Ref. 21), the concave region and unique radii of the NTR electrode are purposely designed to generate ring-directed welding current, which improves weld current density and facilitates the melting of the aluminum alloys from the periphery toward the center of the weld area. In contrast, the RSW process utilizing MRD technology melts the aluminum alloy from the center outward toward the periphery.

This paper developed an optimized NTR electrode for heat-treatment-free die-casting aluminum alloy C611, and preheating and postheating processes were designed to improve weld quality. The effects of welding methods on the microstructure, morphology, and tensile shear strength of welds were studied, which would provide a basis for applying heat-treatment-free cast aluminum alloy. Furthermore, the contact resistance during the welding and the microcosmic properties of the equiaxed grain zone (EGZ) in the weld were measured and analyzed using different welding processes.

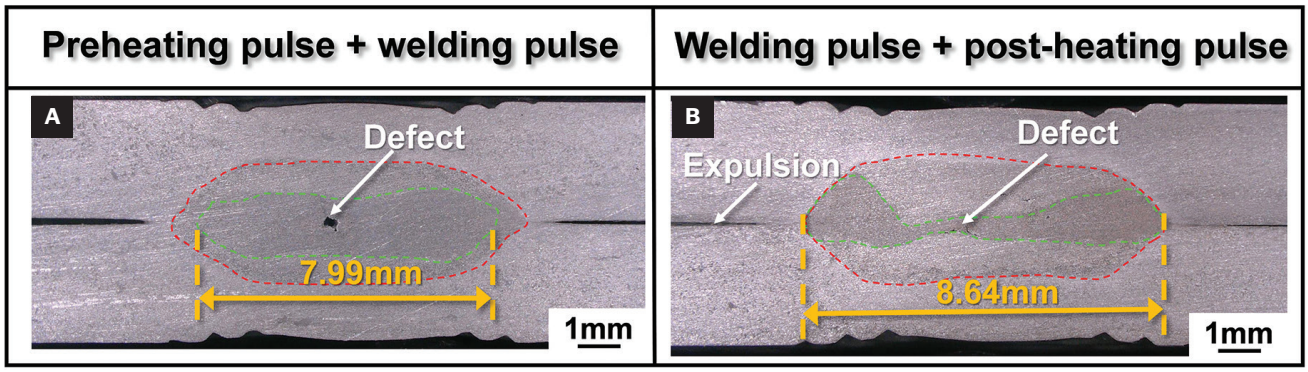

Fig. 5 — A — Preheating pulse + welding pulse; B — welding pulse + postheating pulse.

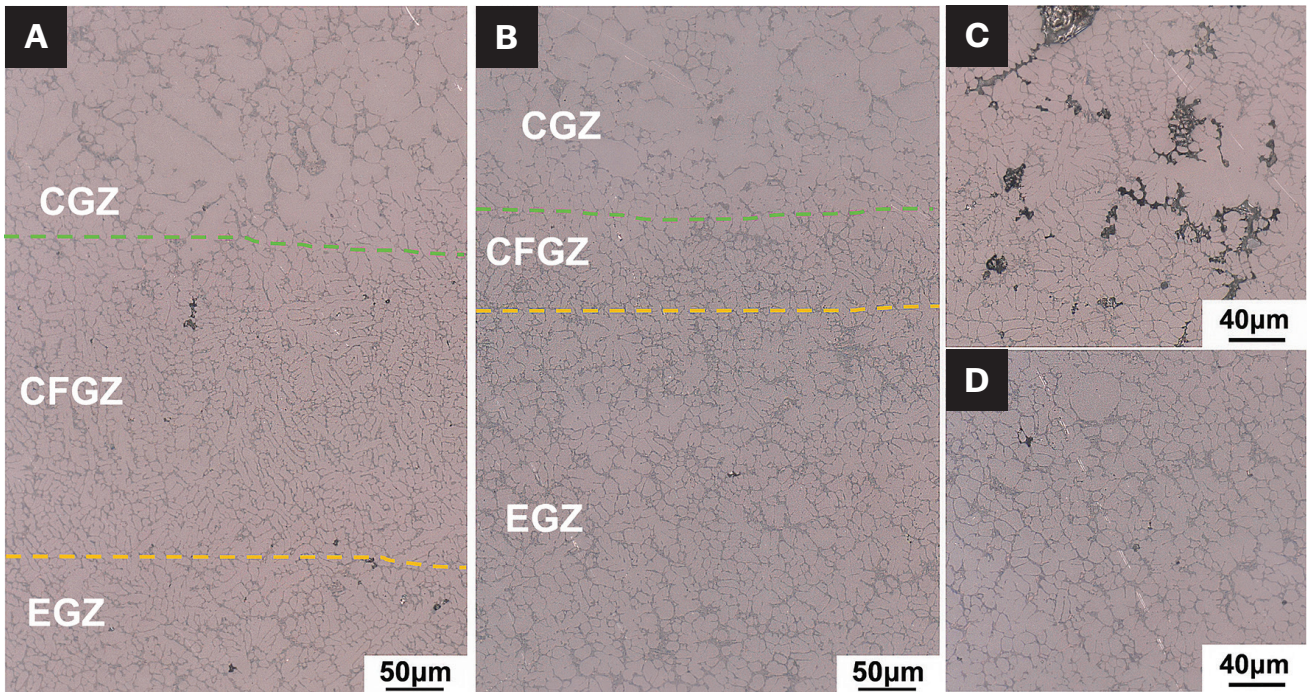

Fig. 6 — Microstructure of nugget: A — Magnified view of region A marked in Fig. 4A; B — magnified view of region B marked in Fig. 4B; C — magnified view of region C marked in Fig. 4A; D — magnified view of region D marked in Fig. 4B.

Experimental Procedures

Materials

This research employed a 3.0-mm-thick commercial heat-treatment-free die-casting aluminum alloy (C611). Table 1 shows its chemical composition and mechanical properties. The electrode was an improved NTR-D electrode based on the NTR electrode (Ref. 24). The electrode had a 12 mm diameter and a curvature of R0 = 30 mm (100 mm before optimization). There was a concave region in the center of R_0, three convex rings with radii of R_1, R_2, and R_{33} were distributed outside the concave ($R_1 < R_2 < R_3$), and the NTR electrode had only two convex rings before optimization — Fig. 1. The electrodes were made of chromium zirconium copper alloy.

Welding Method

A medium-frequency direct current welding system was used. The welding system was comprised of a SIV37 controller, an OBARA welding gun, and a FANUC robot. The flow rate and temperature of the cooling water were kept at 4 L/min and 20°C. Before welding, all aluminum plates and electrode surfaces were cleaned with alcohol to remove grease and contaminants. The test was divided into two groups according to different processes. Process 1 was single pulse welding (as shown in Fig. 2A) with a preloading time of 300 ms, a welding current of 30 kA, and a welding time of 200 ms. For Process 2, the preheating current of 9–18 kA was added based on Process 1, the increasing magnitude was set at 3 kA, the preheating time was 50 ms, and three samples were welded under each condition. When expulsion appeared in

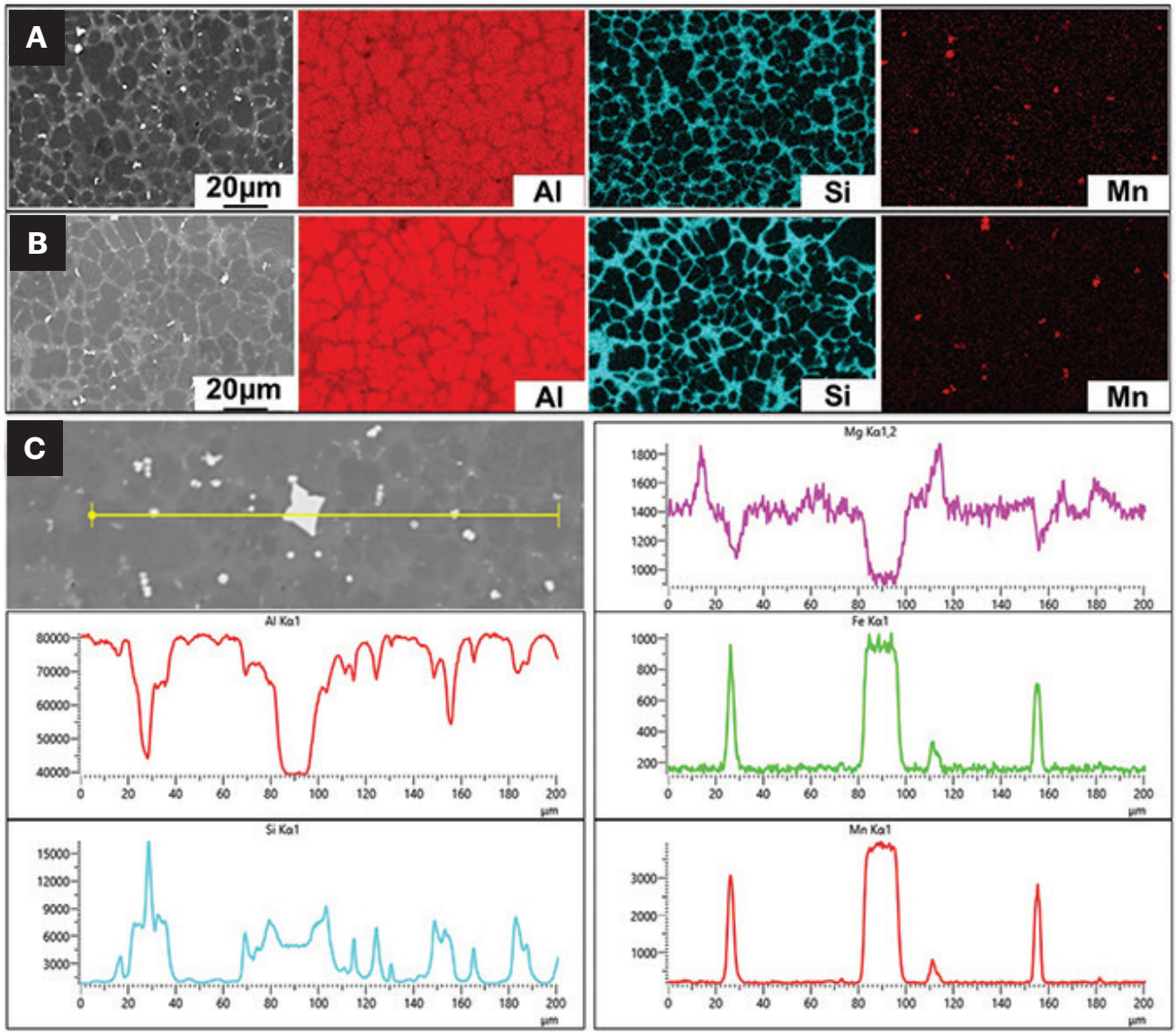

Fig. 7 — The element distribution test of the EGZ in two processes: A — Process 1; B — Process 2; C — line scanning of white particle phase.

Table 2 — Preheating Current Selection Process

Protocol	Preheating Current	Number of Expulsions	Number of No Expulsions
1	9 kA	3	0
2	12 kA	2	1
3	15 kA	1	2
4	18 kA	1	2

at least two samples, the preheating current was considered insufficient to suppress it. The experimental results are shown in Table 2. Expulsion was suppressed when the preheating current was above 12 kA. So, the preheating current was selected as 15 kA. The postheating current was selected as 20kA, greater than the preheating current and less than the welding current. Process 2 added a preheating pulse before the main welding pulse and a postheating pulse after the main welding pulse. Preheating pulse: The preheating time was 50 ms and the preheating current was 15 kA. Postheating pulse: The cooling time before postheating was 10 ms, the postheating current was 20 kA, and the postheating time was 50 ms (as shown in Fig. 2B). The current and contact resistance during the welding process were real-time measured by a welding controller (Miyachi MM-370C), as shown in Fig. 2C. To explore the specific role of postheating and preheating pulse, experiments with a preheating pulse or postheating pulse were carried out.

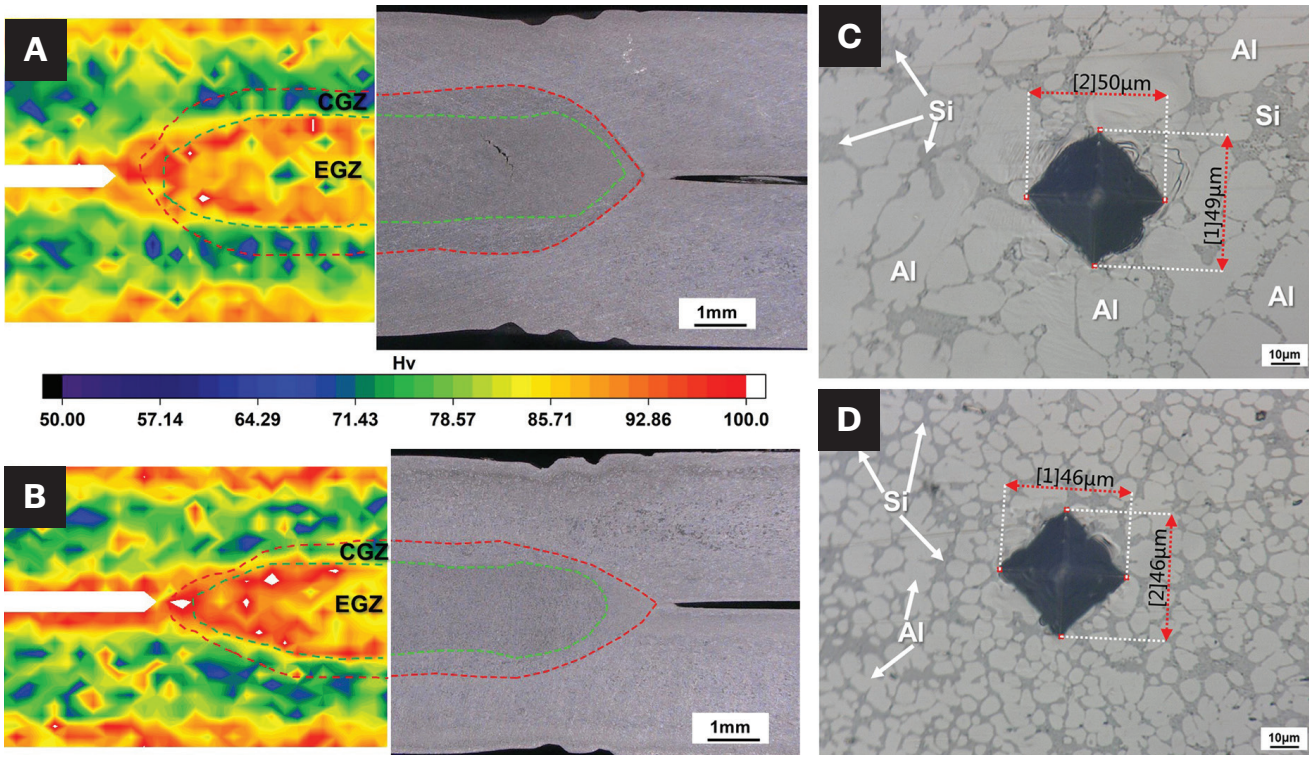

Fig. 8 — Microhardness distribution of joints with different processes: A — Process 1; B — Process 2; C — test point of the CGZ region in Process 1; D — test point of the EGZ region in Process 1.4.

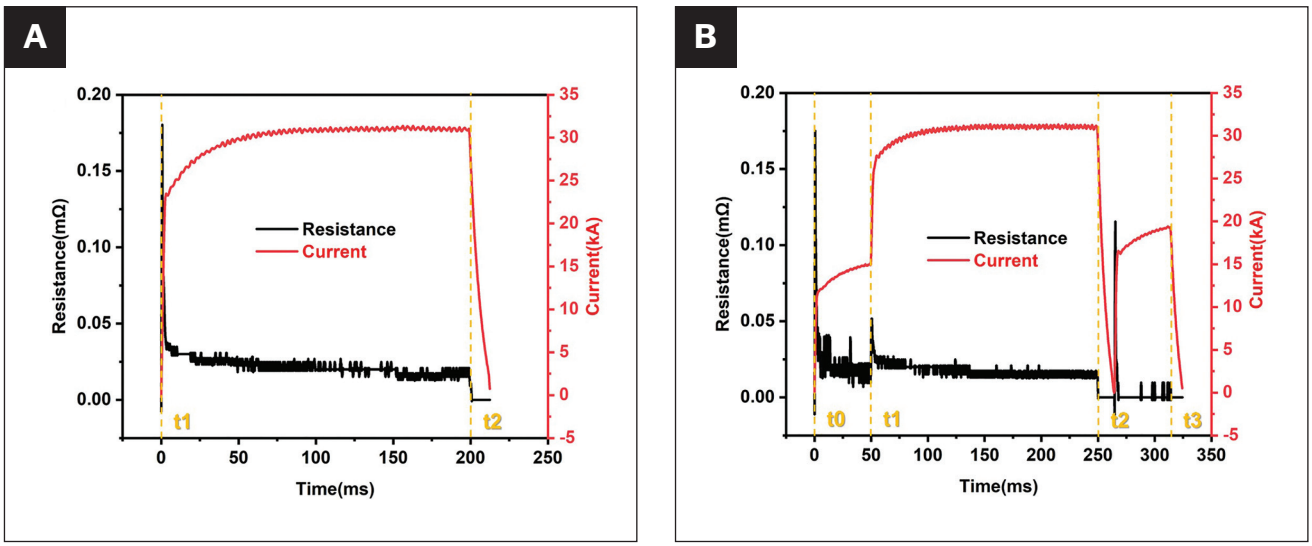

Fig. 9 — Time-current and resistance real-time curves of different processes: A — Process 1; B — Process 2.

Material Characterization and Performance Test

According to AWS D8.2M:2017, *Specification For Automotive Weld Quality–Resistance Spot Welding of Aluminum*, metallographic and mechanical tests were carried out on the joints using two different processes. The morphology and microstructures of the RSW nugget were analyzed using a VHX-6000 optical microscope system produced by KEYENCE in Japan. The element distribution test used the Guoyi 5000 scanning electron microscope with an energy dispersive spectrometer. The weld's microhardness profile was measured using a microhardness tester (VICKERS 402MVD), with a load of 100 g, a hold time of 10 s, and a measurement interval of 200 μm. Fig. 3A shows the size of the tensile shear test sample. The welding spot was in the center of the 38 × 38 mm overlapping area. The weld's tensile shear property was tested on a universal testing machine (UTM5015) with

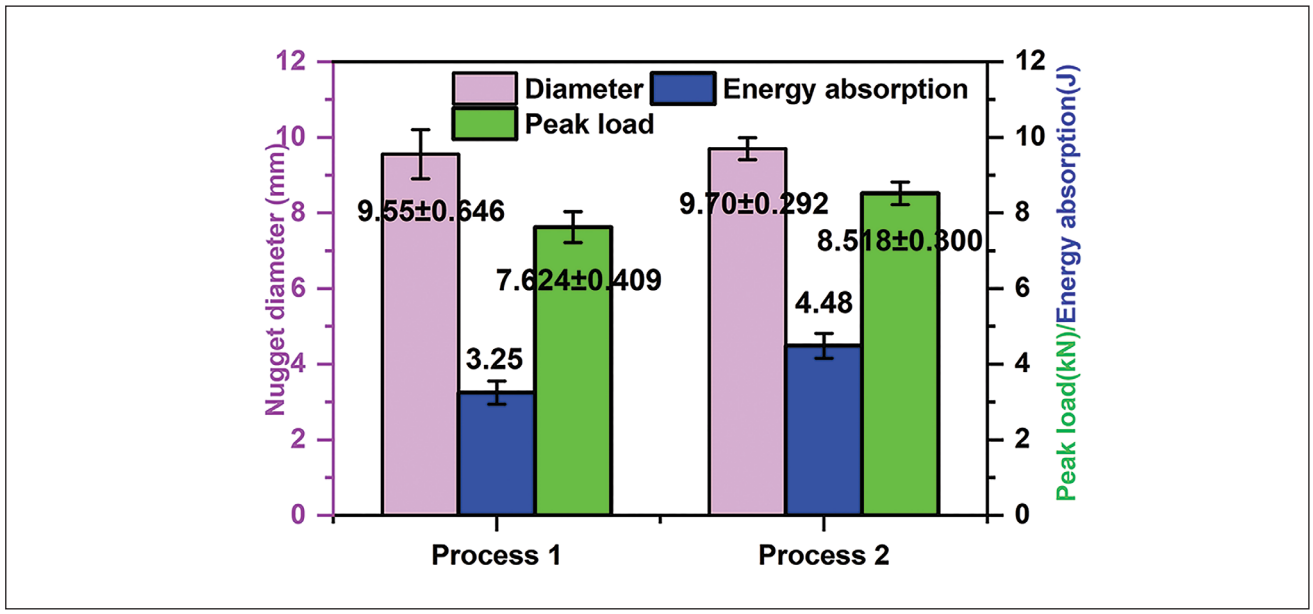

Fig. 10 — Tensile shear property.

a 2 mm/min loading speed. Each group of processes was repeated four times. The nugget size was measured after tensile failure; the measurement method is shown in Fig. 3C. To compare the performance differences of the equiaxed grain zone in the weld under different processes, the microtensile samples (Fig. 3B) were cut from the EGZ by electrical discharge machining technology. The tensile test was conducted on the universal testing machine (UTM5015) with a 0.2 mm/min loading speed. The macromorphology and microstructure of the fractured welds were observed using a KEYENCE VHX-6000 ultra-depth-of-field microscope and a Guoyi 5000 scanning electron microscope.

Results

Morphology

Figs. 4A and B show the nugget morphology with the two processes. The weld surface had an indentation left by the electrode ring and a bulge resulting from the concavity of the electrode center. The nugget produced by the two processes could be divided into three zones, namely the heat-affected zone, columnar grain zone (CGZ), and equiaxed grain zone (Ref. 26). Additionally, the weld nugget created by Process 1 exhibited apparent cracking defects, whereas the nugget from Process 2 was free of such defects. Moreover, expulsion was evident in the nuggets from Process 1.

This paper carried out three sets of welding experiments that used only preheating or postheating pulses to explore the specific functions of preheating and postheating pulses. Fig. 5 shows a large shrinkage defect in the samples with a preheating pulse + welding pulse. The welding pulse + postheating pulse sample shows expulsion and a little shrinkage defect, and the EGZ is a peanut-shaped structure. Therefore, the preheating pulse prevented expulsion, and the postheating pulse could reduce the possibility of welding defects.

Microstructure and Hardness Distribution

Figs. 6A and B are magnified views of regions A and B marked in Figs. 4A and B. It was found that there was a columnar fine grain zone (CFGZ) parallel to the heat dissipation direction at the junction of the EGZ and CGZ in both processes. However, the CFGZ range in Process 2 was smaller. Figs. 6C and D are the EGZ amplification diagrams of the two processes, and the EGZ of parameter 1 had more defects. To explore the composition of the EGZ phase, an element plane distribution scanning of the EGZ of the two processes (Figs. 7A and B) was carried out. It was found that the phase composition of the EGZ region of the two processes was similar, mainly composed of Al and Si phases, and there were also dispersed white particle phases. To further determine the composition of the white particles, an element point scanning of the white particle phase was carried out (Fig. 7C). According to Niklas (Ref. 27), the white particles are AlFeMnSi phase, which can avoid the formation of harmful β-Al_5FeSi compounds and improve the mechanical properties of the alloy.

For the two processes, the hardness distribution of the nugget zone was uneven, as shown in Fig. 8. The hardness of the EGZ was higher than that of the CGZ. As shown in Figs. 8C and D, the hardness point size in the CGZ was larger than in the EGZ, mainly due to the coarse grain size in the CGZ. The hardness of the EGZ of Process 2 was slightly larger than that of Process 1. Because there were many shrinkage defects in the EGZ of Process 1, the hardness would be reduced when the test point was on the shrinkage defects.

Welding Process Analysis

The different parameters of the two processes inevitably led to differences in heat input, resulting in a difference in nuggets. The size of the contact resistance also had a greater impact on the heat input. Fig. 9 shows the real-time current

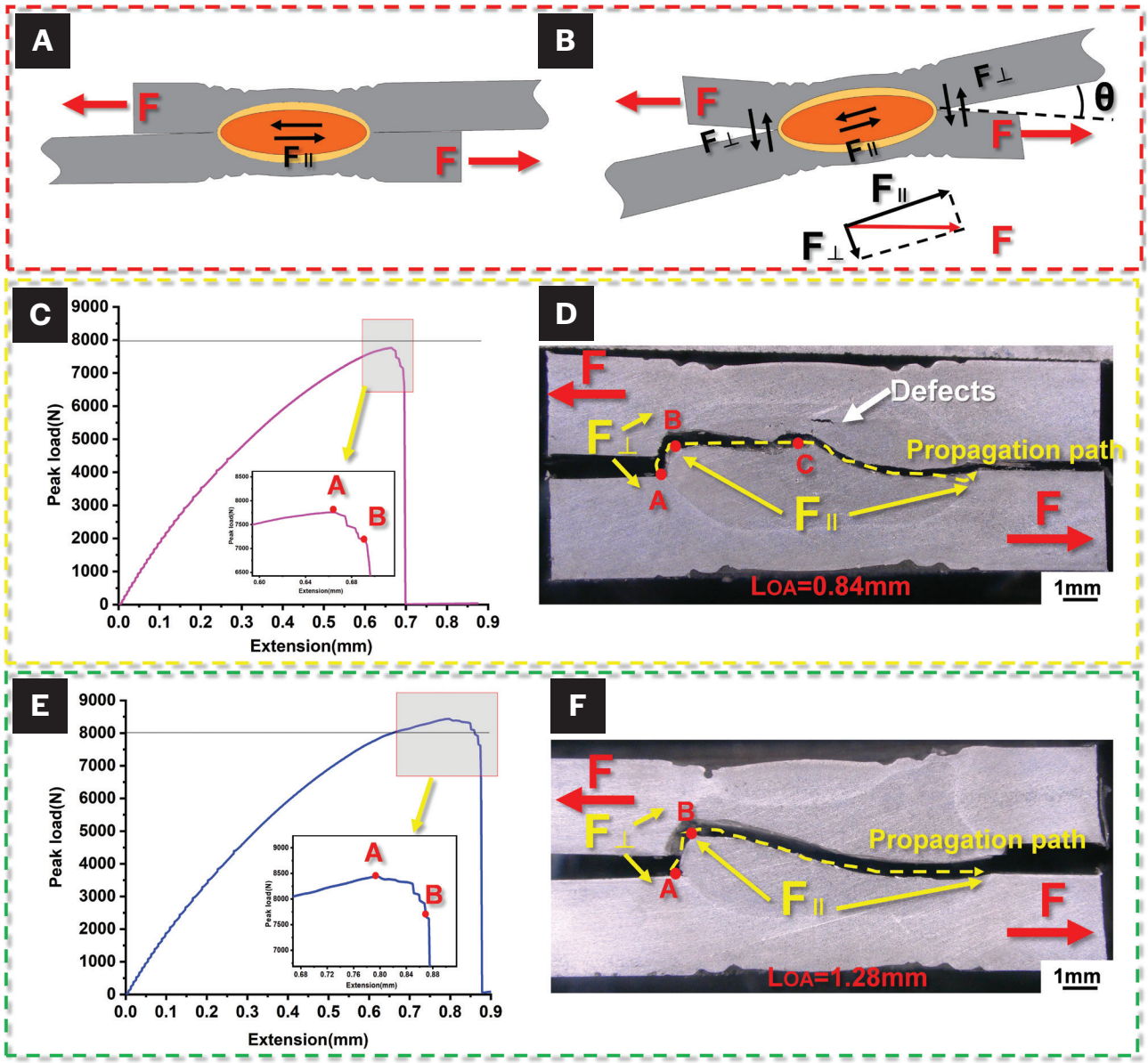

Fig. 11 — Stress diagram of the tensile shear process and load-displacement curve and crack propagation path diagram: A — Small nugget crack propagation path diagram; B — large nugget crack propagation path diagram; C — Process 1 sample displacement-load curve; D — Process 1 specimen fracture section; E — Process 2 displacement-load curve; F — Process 2 specimen fracture section.

and resistance changes of the two processes. At the beginning of the welding pulse, the resistance of the t1 stage of Process 1 (0.18 mΩ) was greater than the resistance of Process 2 (0.05 mΩ). It showed that a preheating pulse can effectively reduce contact resistance.

Tensile Shear Tests

Fig. 10 shows the two processes' nugget diameter, tensile shear peak load, and energy absorption. Energy absorption was obtained by calculating the area of the peak load under the load-displacement curve (Ref. 29). The nugget diameter of Process 2 was 9.7 mm, and the nugget diameter of Process 1 was 9.55 mm, as shown in Fig. 10A. There was little difference in the nugget diameter. The peak load of Process 2 was 8518 N, which was 11.7% larger than the peak load of Process 1. The energy absorption of 4.48 J of Process 2 was also greater than the 3.24 J of Process 1, an increase of 38.3%. According to Refs. 30 and 31, the nugget diameter tended to be directly proportional to the tensile shear strength, and it showed that the nugget strength of Process 2 was greater than that of Process 1.

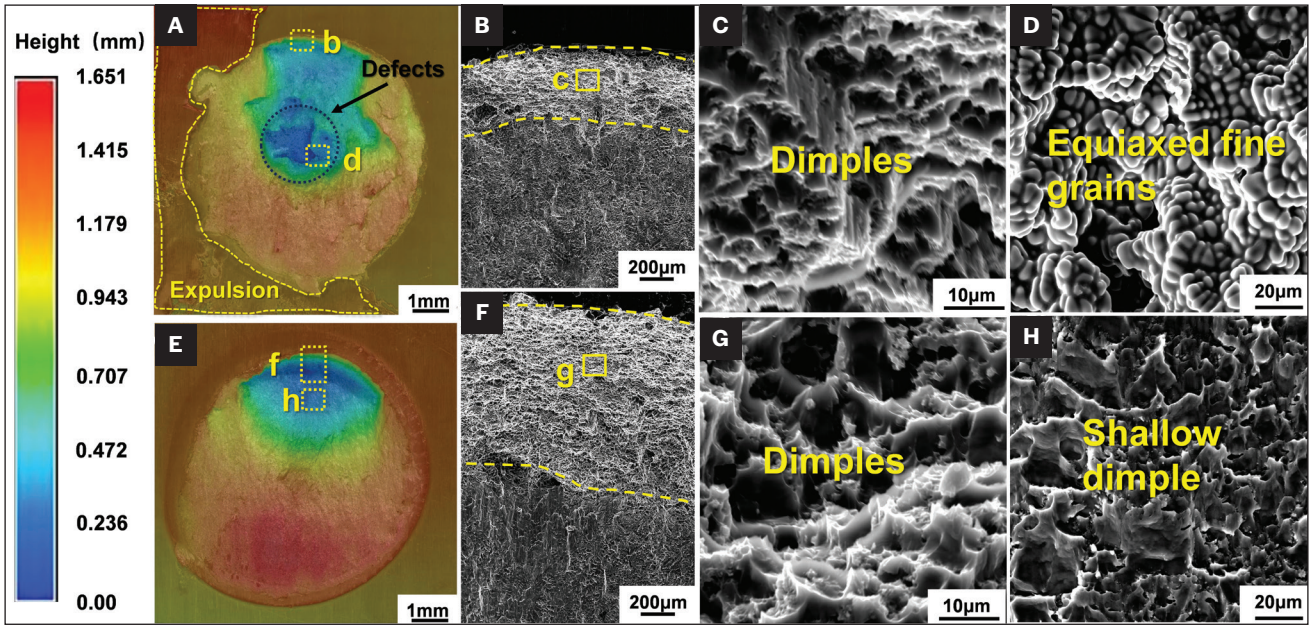

Fig. 12 — Processes 1 and 2 fracture morphology: A — Macroscopic fracture morphology of Process 1; B — magnified view of region b marked in Fig. A; C — magnified view of region c marked in Fig. B; D — magnified view of region d marked in Fig. A; E — macroscopic fracture morphology of Process 2; F — magnified view of region f marked in Fig. E; G — magnified view of region g marked in Fig. F; H — magnified view of region h marked in Fig. E.

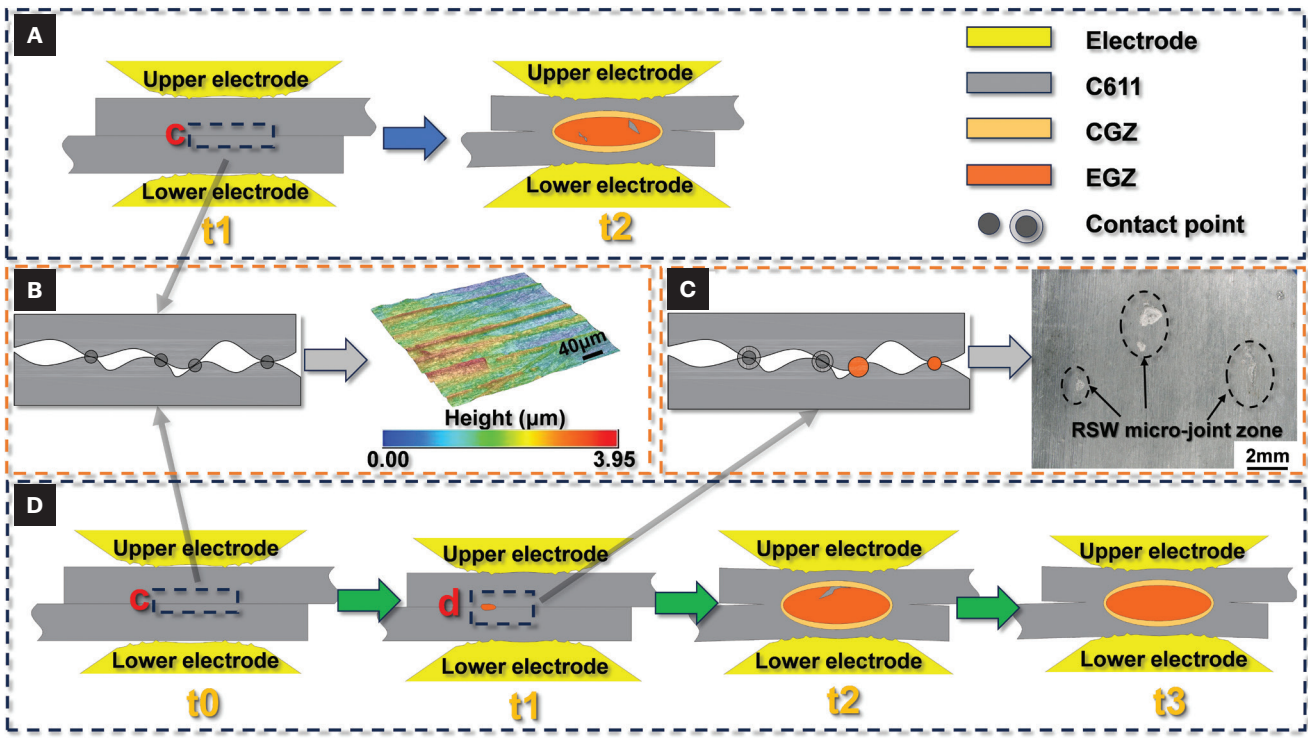

Fig. 13 — RSW process diagram of Processes 1 and 2: A — Process 1; B — C611 surface magnification map; C — surface morphology of plate after preheating pulse; D — Process 2.

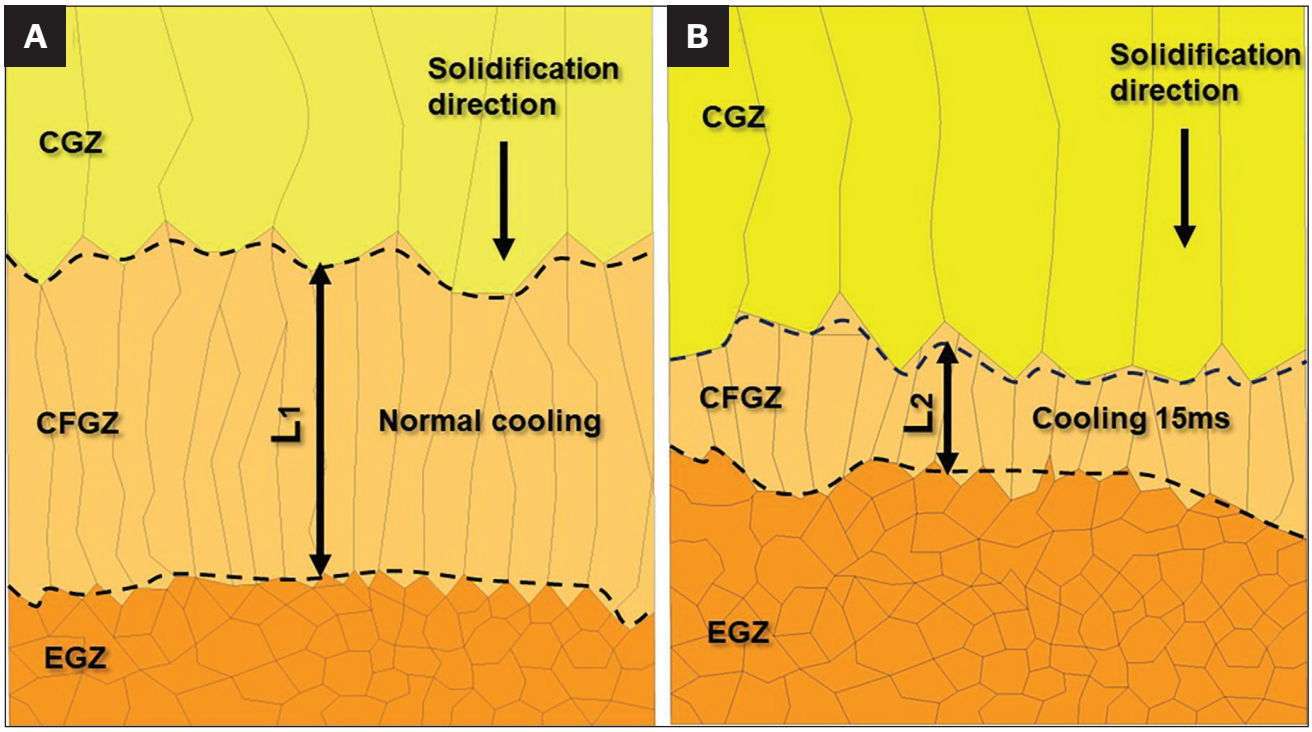

Fig. 14 — The solidification process of the CGZ and EGZ in two processes: A — Process 1; B — Process 2.

Discussion

Failure Analysis

Figs. 11A and B schematically show the stress evolution of the welded joint during the tensile process. According to Zhang's research (Ref. 32), the welded joint of the RSW specimen was first subjected to the shear stress ($F_{\parallel}$) parallel to the tensile direction during the tensile shear process (Fig. 11A). To align with the direction of the applied force, the nugget rotated to a certain extent, so the tensile stress ($F_{\perp}$) perpendicular to the tensile direction was generated (Fig. 11B). According to Pouranvari (Ref. 33), the fracture mode of resistance spot welding could be divided into three types: interfacial failure (IF), pull-out failure (PF), and partial interfacial failure (PIF). The driving force of IF is the shear stress, and the driving force of PF is the tensile stress. The force between shear stress and tensile stress produces PIF, which results from competition between IF and PF and is related to rotation. The greater the rotation angle, the greater the tendency of PF (Refs. 32, 34, 35).

Figs. 11D and F depict each process's tensile shear fracture cross sections. The fracture modes of the two processes were similar — both IF — but there was a PF tendency in the initial crack propagation stage. The failure driving force tended to move from shear stress to tensile stress. The crack started from point A and extended to point B. As the tension proceeded, the driving force turned to shear stress, the crack propagated along the parallel tensile direction, and finally, interfacial failure occurred. Although the crack propagation paths of the two processes were similar, the crack propagation path L_{AB} = 1.28 mm under the tensile stress of Process 2 was larger than that of Process 1 (L_{AB} = 0.84 mm). The peak load and tensile displacement of Process 2 were larger than those of Process 1, as shown in Figs. 11C and E. The crack of Process 1 propagated along the tensile direction after the B point, and the crack returned to the nugget center after the C point. However, the crack of Process 2 directly returned to the nugget center after the B point. This was mainly due to the decreased strength of the nugget structure at the nugget center. According to the hardness distribution in Figs. 8A and B, the hardness of the nugget center was slightly lower than that of both ends of the nugget.

Fig. 12 shows the fracture morphology of Processes 1 and 2. The nugget fracture of Process 1 had a significant expulsion and some defects in the nugget center (Fig. 12A). In contrast, the nugget fracture of Process 2 had no expulsion and defects (Fig. 12E). The initial crack propagation stage AB of Processes 1 and 2 are shown in Figs. 12B and F. By comparison, the initial crack propagation stage of Process 2 was larger, and the apparent dimples could be observed, as shown in Figs. 12C and G. Equiaxed, fine grains (Fig. 12D) were observed around the defects of Process 1 (the position of point C in Fig. 11D), which was direct evidence of solidification shrinkage defects (Ref. 35). The appearance of a shrinkage cavity reduced the performance of the weld because the crack of Process 1 in Fig. 11D propagated to point C after point B. Shallow dimples can be observed in the fractured part after point B of Process 2, which differed from Process 1.

Preheating Pulse

The preheating pulse can effectively reduce the contact resistance at the initial stage of the welding pulse, as shown

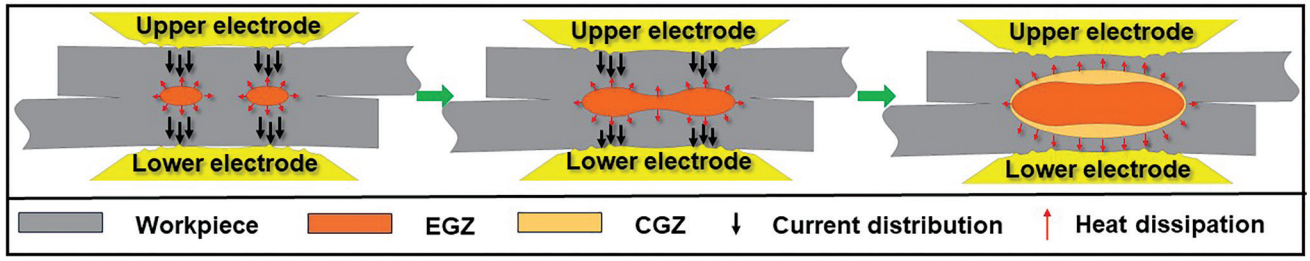

Fig. 15 — The nugget formation process of the NTR electrode.

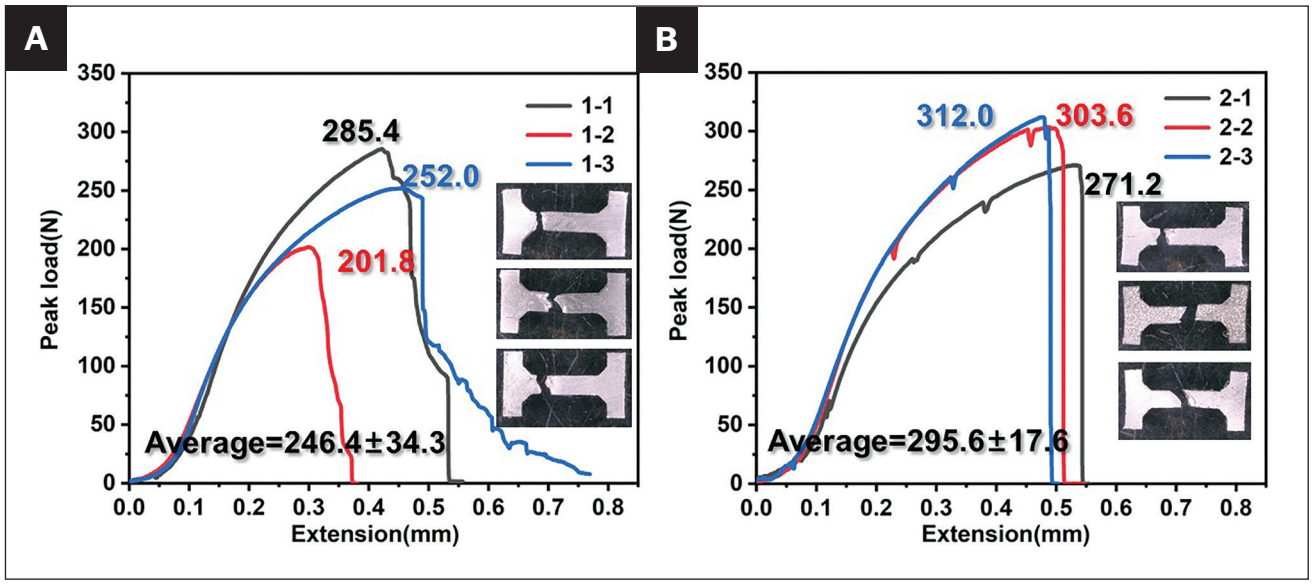

Fig. 16 — The displacement-load curve of the EGZ specimen: A — Process 1; B — Process 2.

in Fig. 9. For Process 1, there was a squeeze stage before the welding pulse was introduced. The contact resistance was mainly from the two aluminum plates. The resistance was large because the plate's surface was uneven (Fig. 13B), and the contact surface at the welding area was a point contact. For Process 2, as the preheating pulse was added, the point contact between the two plates could be melted to form a micro-joint zone (Fig. 13C), significantly reducing the contact resistance. The heat generation of RSW is based on Joule's law, which is expressed as follows (Ref. 36):

$$Q = I^2(R_{WW} + 2R_{EW} + R_W)t$$

where Q is the total heat input, t is the welding time, I is the welding current, and R_{WW}, R_{EW}, and R_W are the contact resistance between the workpiece, the contact resistance between the electrode and the workpiece, and the bulk resistance of the base metal, respectively.

When the welding current I and the welding time t were the same, the greater the total contact resistance, the greater the heat input Q. Therefore, when the welding pulse was carried out, the initial heat input of Process 1 was larger. This made Process 1 more prone to expulsion.

Postheating Pulse

The previous results showed that the postheating pulse greatly influenced the solidification of the nugget, which affected the morphology and structure of the nugget. Fig. 14 describes the solidification process of the CGZ and EGZ in the two processes. For Process 1, the nugget temperature was higher after the welding pulse, and the temperature gradient was larger. Therefore, a CFGZ with a width of L_1 was formed at the junction of CGZ and EGZ (Fig. 14A). According to Deng (Ref. 37), when the welding current was disconnected for 30 ms, the nugget was only partially solidified at the edge, and most of the nugget was still liquid. Therefore, the cooling time was 15 ms before the postheating pulse in Process 2. Only a small range of (L_2 width) CFGZ was formed at the junction of the CGZ and EGZ (Fig. 14B). According to Bamberg's research (Ref. 38), reducing the range of the columnar crystal zone in the nugget improves the tensile shear properties of aluminum alloy resistance spot welded joints. Besides, the postheating pulse prolonged the flow time of the liquid metal in the nugget, which was beneficial for filling the shrinkage cavity and crack defects in the nugget.

It can be seen from Fig. 5 that there were fewer defects in the nugget of the preheating pulse + welding pulse sample. The EGZ center depression of the welding pulse + postheating

pulse nugget made its EGZ similar to the peanut-like shape, but the size of the EGZ (8.64 mm) was still larger than that of the preheating pulse + welding pulse sample (7.99 mm). This was mainly because the welding pulse + postheating pulse sample produced a large splash and took away a large amount of heat. Secondly, due to the special nucleation mode of the NTR electrode (Fig. 15) and the particular end-face morphology of the NTR electrode, the nugget preferentially nucleated on the convex ring (R_1) and then expanded to the nugget center until the nugget filled the entire plate welding end face to form a complete nugget, which is called ring-shaped nucleation (Ref. 25). However, when the heat input was insufficient, the nugget found filling the whole plate welding end face difficult, so the nugget was peanut-like.

Mechanical Properties

From the results of tensile shear, the tensile shear peak load of Process 2 was larger, mainly because the nugget hardness of Process 2 was greater than that of Process 1 (Figs. 8A and B). According to the existing reports (Refs. 39, 40), the peak load of tensile shear in IF mode only depends on the nugget size and hardness. So, increasing nugget size or hardness promotes the tensile shear peak load. The microtensile samples of the two processes were taken from the EGZ for a deeper understanding. The results are shown in Fig. 16. Results showed that the displacement-load curve of the EGZ of Process 2 was more consistent, and the average peak load of Process 2 (295.6 N) was 20% higher than that of Process 1 (246.4 N). This shows that the higher the hardness, the greater the organizational strength.

Conclusion

In this study, the improved NTR electrode combined with the preheating and postheating process was used to solve the problems of poor stability of resistance spot welded joints and defects formation in a nugget of heat-treatment-free die-casting aluminum alloy C611. The resistance spot welding process controlled the nucleation process, and the nugget morphology, microstructure, and tensile shear properties were analyzed and compared. The following conclusions are drawn:

1. Adding a preheating pulse made the plate realize micro-connection, reducing and stabilizing the plate's contact resistance. The decrease in contact resistance reduced the initial heat generation of the welding pulse, resulting in a lower heat generation. Therefore, the occurrence of expulsion could be effectively reduced.

2. The addition of a postheating pulse could reduce the width of the CFGZ and increase the flow time of the liquid metal so that the liquid metal had enough time to fill the defects, such as shrinkage and cracks in the nugget, that could be suppressed.

3. The preheating pulse and postheating pulse significantly improved the strength of the EGZ's structure so that the weld's tensile shear peak load and energy absorption were increased by 11.7% and 38.3%, respectively.

4. The NTR electrode's annular nucleation could stabilize the EGZ region's size.

Acknowledgments

The authors thank the financial support of the Shanghai 2023 Science and Technology Innovation Action Plan Natural Science Foundation Project (Grant No. 23ZR1462900), the "Tip Spear" and "Guiding Goose" R&D Campaign of Zhejiang Province (Grant No. 2022C01026), the Shanghai Prospective Innovation Research Institute project (Grant No. 22xtcx00500), and the Project (Grant No. HCXBCY-2023-021).

References

1. Kim, H. C., and Wallington, T. J. 2013. Life-cycle energy and greenhouse gas emission benefits of lightweighting in automobiles: Review and harmonization. *Environmental Science & Technology* 47(12): 6089–6097. DOI: 10.1021/es3042115

2. Humpenöder, F., Popp, A., Stevanovic, M., et al. 2015. Land-use and carbon cycle responses to moderate climate change: Implications for land-based mitigation? *Environmental Science & Technology* 49(11): 6731–6739. DOI: 10.1021/es506201r

3. Modaresi, R., Pauliuk, S., Løvik, A. N., et al. 2014. Global carbon benefits of material substitution in passenger cars until 2050 and the impact on the steel and aluminum industries. *Environmental Science & Technology* 48(18): 10776-10784. DOI: 10.1021/es502930w

4. Fu, P., Peng, L., and Ding, W. 2018. Automobile lightweight technology: Development trends of aluminum/magnesium alloys and their forming technologies. *Strategic Study of Chinese Academy of Engineering* 20(1): 84–90. DOI: 10.15302/J-SSCAE-2018.01.012

5. Kawajiri, K., Kobayashi, M., and Sakamoto, K. 2020. Lightweight materials equal lightweight greenhouse gas emissions?: A historical analysis of greenhouse gases of vehicle material substitution. *Journal of Cleaner Production* 253: 119805. DOI: 10.1016/j.jclepro.2019.119805

6. Luo, Z., Ao, S., Chao, Y. J., et al. 2015. Application of pre-heating to improve the consistency and quality in AA5052 resistance spot welding. *Journal of Materials Engineering and Performance* 24: 3881–3891. DOI: 10.1007/s11665-015-1704-x

7. Cui, L. H., Qiu, R. F., Shi, H. X., et al. 2014. Resistance spot welding between copper coated steel and aluminum alloy. *Applied Mechanics and Materials* 675: 19–22. DOI: 10.4028/www. scientific.net/AMM.675-677.19

8. Florea, R. S., Solanki, K. N., Bammann, D. J., et al. 2012. Resistance spot welding of 6061-T6 aluminum: Failure loads and deformation. *Materials & Design* 34: 624–630. DOI: 10.1016/j.matdes.2011.05.017

9. Winters, J. 2014. Light vehicles' lightweight future. *Mechanical Engineering-CIME* 136(8): 11–12.

10. Nellippallil, A. B., De, P. S., Gupta, A., et al. 2017. Hot rolling of a non-heat treatable aluminum alloy: Thermo-mechanical and microstructure evolution model. *Transactions of the Indian Institute of Metals* 70: 1387–1398. DOI: 10.1007/s12666-016-0935-3

11. Glazoff, M. V., Khvan, A., Zolotorevsky, V. S., et al. 2018. *Casting aluminum alloys: Their physical and mechanical metallurgy*. Butterworth-Heinemann.

12. Aluminum Association. 1984. *Aluminum: Properties and physical metallurgy*. ASM International.

13. Li, B., Wang, Y., and Gao, B. 2021. Extraction of Al from coarse Al–Si alloy by the selective liquation method. *Materials* 14(13): 3680. DOI: 10.3390/ma14133680

14. Yu, L., Jiang, S., Cao, F., et al. 2021. Thermal expansion behavior of Co-spray formed Al-20Si/7075 bimetallic gradient alloy. *Materials* 14(15): 4100. DOI: 10.3390/ma14154100

15. Akhter, R., Ivanchev, L., and Burger, H. P. 2007. Effect of pre/post T6 heat treatment on the mechanical properties of laser welded

SSM cast A356 aluminium alloy. *Materials Science and Engineering: A* 447(1–2): 192–196. DOI: 10.1016/j.msea.2006.10.148

16. Reisgen, U., Senger, A., and Olschok, S. 2018. Electron beam welding in atmosphere of aluminum die casting alloys made of different qualities. *Welding in the World* 62: 1207–1213. DOI: 10.1007/s40194-018-0640-4

17. Scheibner, S., Tragl, W., Treitler, R, et al. 2006. Welding suitability of pressure die casting aluminium components. *ATZ Worldwide* 108(9): 19–22. DOI: 10.1007/BF03224849

18. Vivas, J., Fernández-Calvo, A. I., Aldanondo, E., et al. 2022. Friction stir weldability at high welding speed of two structural high-pressure die casting aluminum alloys. *Journal of Manufacturing and Materials Processing* 6(6): 160. DOI: 10.3390/jmmp6060160

19. Wan, Z., Wang, H. P., Wang, M., et al. 2016. Numerical simulation of resistance spot welding of Al to zinc-coated steel with improved representation of contact interactions. *International Journal of Heat and Mass Transfer* 101: 749–763. DOI: 10.1016/j.ijheatmasstransfer.2016.05.023

20. Chantasri, S., Poonnayom, P., Kaewwichit, J., et al. 2015. Effect of resistance spot welding processes on AA1100 aluminum alloy and SGACD zinc coated lap joint properties. *International Journal of Advanced Culture Technology* 3(1): 153–160. DOI: 10.17703/IJACT.2015.3.1.153

21. Deng, L., Li, Y. B., Carlson, B. E., et al. 2018. Effects of electrode surface topography on aluminum resistance spot welding. *Welding Journal* 97(4): 120-s to 132-s. DOI: 10.29391/2018.97.011

22. Wang, Y., Tao, W., and Yang, S. 2019. A method for improving joint strength of resistance spot welds of AA 5182-0 aluminum alloy. *Journal of Manufacturing Processes* 45: 661–669. DOI: 10.1016/j.jmapro.2019.07.024

23. Wang, Y., and Yang, S. 2022. Effects of electrode combinations on RSW of 5182-O/AlSi10MnMg aluminum. *Welding Journal* 101 (2): 54-s to 66-s. DOI: 10.29391/2022.101.005

24. Shanglu, Y., Yanjun, W., and Wu, T. 2024. Resistance spot welding electrode cap. U.S. Patent 11890701, filed Dec. 18, 2018, and issued Feb. 6, 2024.

25. Li, M., Wang, Y., Yang, S., et al. 2021. Improving mechanical properties and electrode life for joining aluminum alloys with innovatively designated Newton ring electrode. *Journal of Manufacturing Processes* 64: 948–959. DOI: 10.1016/j.jmapro.2021.02.001.

26. Li, Y., Shan, H., Zhang, Y., et al. 2017. Failure mode of spot welds under cross-tension and coach-peel loads. *Welding Journal* 96 (11): 413-s to 420-s.

27. Niklas, A., Baquedano, A., Orden, S., Nogués, E., Da Silva, M. and Fernández-Calvo, A.I. 2016. Microstructure and Mechanical properties of a new secondary AlSi10MnMg (Fe) alloy for ductile high pressure die casting parts for the automotive industry. *Key Engineering Materials* 710: 244–249. DOI: 10.4028/www.scientific.net/kem.710.244

28. Zeren, M. 2005. Effect of copper and silicon content on mechanical properties in Al–Cu–Si–Mg alloys. *Journal of Materials Processing Technology* 169 (2): 292–298. DOI: 10.1016/j.jmatprotec.2005.03.009

29. Zhang, H., and Senkara, J. 2011. *Resistance welding: Fundamentals and applications*. CRC Press.

30. Florea, R. S., Solanki, K. N., Bammann, D. J., et al. 2012. Resistance spot welding of 6061-T6 aluminum: Failure loads and deformation. *Materials & Design* 34: 624–630. DOI: 10.1016/j.matdes.2011.05.017

31. Li, Y., Zhang, Y., Luo, Z., et al. 2016. Failure mode transition of triple-thin-sheet aluminum alloy resistance spot welds under tensile-shear loads. *Welding Journal* 95: 479-s to 490-s.

32. Zhang, H., Qiu, X., Xing, F., Bai, J., and Chen, J. 2014. Failure analysis of dissimilar thickness resistance spot welded joints in dual-phase steels during tensile shear test. *Materials & Design* 55: 366–372. DOI: 10.1016/j.matdes.2013.09.040

33. Pouranvari, M., and Marashi, S. P. H. 2011. Failure mode transition in AHSS resistance spot welds. Part I. Controlling factors. *Materials Science and Engineering: A* 528(29–30): 8337–8343. DOI: 10.1016/j.msea.2011.08.017

34. Pouranvari, M., Asgari, H. R., Mosavizadch, S. M., Marashi, P. H., and Goodarzi, M. 2007. Effect of weld nugget size on overload failure mode of resistance spot welds. *Science and Technology of Welding and Joining* 12(3): 217–225. DOI: 10.1179/174329307x164409

35. Chao, Y. J. 2003. Ultimate strength and failure mechanism of resistance spot weld subjected to tensile, shear, or combined tensile/shear loads. *Journal of Engineering Materials and Technology* 125(2): 125–132. DOI: 10.1115/1.1555648

36. Wang, Y., Mo, Z., Feng, J., and Zhang, Z. 2007. Effect of welding time on microstructure and tensile shear load in resistance spot welded joints of AZ31 Mg alloy. *Science and Technology of Welding and Joining* 12(8): 671–676. DOI: 10.1179/174329307X238380

37. Deng, L., Li, Y., Cai, W., Haselhuhn, A. S., and Carlson, B. E. 2020. Simulating thermoelectric effect and its impact on asymmetric weld nugget growth in aluminum resistance spot welding. *Journal of Manufacturing Science and Engineering* 142(9): 091001. DOI:10.1115/1.4047243

38. Bamberg, P., Gintrowski, G., Liang, Z., Schiebahn, A., Reisgen, U., Precoma, N., and Geffers, C. 2021. Development of a new approach to resistance spot weld AW-7075 aluminum alloys for structural applications: an experimental study–Part 1. *Journal of Materials Research and Technology* 15: 5569–5581. DOI: 10.1016/j.jmrt.2021.10.142

39. Oikawa, H., Murayama, G., Sakiyama, T., Takahashi, Y., and Ishikawa, T. 2006. Resistance spot weldability of high strength steel (HSS) sheets for automobiles. *Shinnittetsu Giho* 385: 36.

40. Alizadeh-Sh, M., Marashi, S. P. H., and Pouranvari, M. 2014. Microstructure–properties relationships in martensitic stainless steel resistance spot welds. *Science and Technology of Welding and Joining* 19(7): 595–602. DOI: 10.1179/ 1362171814Y.0000000230

YUNMING ZHU and **ZHENGQIANG ZHU** *(zhuzhq01@126.com)* are with Nanchang University, College of Advanced Manufacturing, Nanchang, China. **YANJUN WANG**, **JINGYU BAI**, **SHANGLU YANG** *(shangluyang_lab@126.com)*, and **YUNMING ZHU** are with Shanghai Institute of Optics and Fine Mechanics, Chinese Academy of Sciences, Shanghai, China. **WANG** and **YANG** are also with Center of Materials Science and Optoelectronics, University of Chinese Academy of Sciences, Beijing, China. **YUNMING ZHU** and **ZHENGQIANG ZHU** are also with Jiangxi Provincial Key Laboratory of Robot and Welding Automation, Jiangxi, China. **BOYI ZENG** is also with Shien-Ming Wu School of Intelligent Engineering, South China University of Technology, Guangzhou, China.